1-1-2006

Near-Infrared and the Inner Regions of Protoplanetary Disks

Dejan Vinković
Institute for Advanced Study

Željko Ivezić
University of Washington

Tomislav Jurkić
University of Zagreb, Croatia

Moshe Elitzur
University of Kentucky, moshe@pa.uky.edu

The Astrophysical Journal, 636:348–361, 2006 January 1

NEAR-INFRARED AND THE INNER REGIONS OF PROTOPLANETARY DISKS

Dejan Vinković
Institute for Advanced Study, School of Natural Sciences, Einstein Drive, Princeton, NJ 08540; dejan@ias.edu

Željko Ivezić
Department of Astronomy, University of Washington, Seattle, WA 98195; ivezic@astro.washington.edu

Tomislav Jurkić
Department of Physics, Faculty of Science, University of Zagreb, Bijenička 32, HR-10002 Zagreb, Croatia

and

Moshe Elitzur
Department of Physics and Astronomy, University of Kentucky, Lexington, KY 40506; moshe@pa.uky.edu
Received 2005 June 6; accepted 2005 September 7

ABSTRACT

We examine the "puffed-up inner disk" model proposed by Dullemond, Dominik, & Natta for explaining the near-IR excess radiation from Herbig Ae/Be stars. Detailed model computations show that the observed near-IR excess requires more hot dust than is contained in the puffed-up disk rim. The rim can produce the observed near-IR excess only if its dust has perfectly gray opacity, but such dust is in conflict with the observed 10 μm spectral feature. We find that a compact ($\sim$10 AU), tenuous ($\tau_V \lesssim 0.4$), dusty halo around the disk inner regions contains enough dust to readily explain the observations. Furthermore, this model also resolves the puzzling relationship noted by Monnier & Millan-Gabet between luminosity and the interferometric inner radii of disks.

Subject headings: accretion, accretion disks — circumstellar matter — dust, extinction — stars: pre–main-sequence

1. INTRODUCTION

Processes in the immediate vicinity of young pre-main-sequence stars influence the initial stellar evolution and the formation of terrestrial planets. Since small scales of several astronomical units around a star are difficult to resolve, we still lack a clear understanding of processes such as disk accretion, the launching of bipolar jets and winds, and the dynamics and reprocessing of dust in the inner hot disk regions. The dust geometry is one of the basic ingredients needed for constraining theoretical models of these processes. Traditionally, this geometry has been deduced from the spectral energy distribution (SED), which is dominated at infrared wavelengths by dust emission.

A widely popular geometrical description is the two-layered flared-disk model developed by Chiang & Goldreich (1997, hereafter CG97). The model gives a simple method for estimating the flux from the optically thin surface layer of an optically thick disk directly exposed to the stellar radiation and from the colder disk interior heated by the warmer surface. The simplicity of the method, together with evidence for the existence of disks based on radio imaging, made this model a dominant description of T Tau and Herbig Ae/Be stars (HAEBEs; the intermediate-mass, $1.5 \lesssim M_*/M_\odot \lesssim 10$, counterparts of T Tau stars).

Although the CG97 model successfully explains the observed SEDs, advances in imaging techniques revealed shortcomings of this model. Analyzing images at scattering and dust emission wavelengths, Miroshnichenko et al. (1999) concluded that disks alone cannot explain the imaging observations, at least not for some HAEBEs. Instead they modeled the SED with an optically thin halo surrounding an optically thick disk and emphasized that only multiwavelength imaging can distinguish between this and the CG97 model. Subsequent detailed modeling of imaging data in numerous systems revealed the existence of dusty halos around the putative flared disks (Gómez & D'Alessio 2000; Schneider et al. 2003; Stapelfeldt et al. 2003). The inadequacy of the SED as the sole analysis tool in determining the geometry was further demonstrated by Vinković et al. (2003, hereafter V03). They showed that the mathematical expression for the SED calculation in the CG97 model can be transformed into that for the halo-embedded disk and vice versa. This has far-reaching consequences for all studies based solely on SEDs. If not supported by imaging at various wavelengths, SED models can lead to erroneous conclusions about the spatial distribution of dust.

The disk inner region in HAEBEs (within $\sim$10 AU from the star) proved to be more complicated than the original CG97 model. Thermal dust emission from this region peaks at short wavelengths, creating a near-IR bump ($1\ \mu\mathrm{m} < \lambda < 8\ \mu\mathrm{m}$) in the SED of many HAEBEs (Hillenbrand et al. 1992). Chiang et al. (2001) noticed that the CG97 model did not produce enough near-IR flux to explain the bump. This implies that the disk flaring, which increases the emitting volume of the optically thin disk surface, is too small at the inner radii. Since the disk geometry is constrained by vertical hydrostatic equilibrium, an additional hot dust component is required for explaining the near-IR bump. To solve this problem, Dullemond et al. (2001, hereafter DDN01) proposed modifying the CG97 geometry without introducing an additional component. They noted that the disk vertical height is increased (puffed up) at its inner rim because there the disk interior is directly exposed to stellar radiation and is hotter than in the CG97 model at the same radius. The rim is the hottest region of the disk, and with its increased size it is possible to boost the near-IR flux. This puffing of the rim is equivalent to the disk extra flaring that was identified as missing in the CG97 model by Chiang et al. (2001).

Evidence in support of the DDN01 model was garnered from SED modeling of a large sample of HAEBEs (Dominik et al.

2003) and recently also of T Tau stars (Muzerolle et al. 2003). Still, the inner disk geometry remains controversial. Recent advances in near-IR interferometry provide imaging data of this region, and the first results from a large sample of HAEBEs show that many of these objects appear close to circular symmetry (Millan-Gabet et al. 2001; Eisner et al. 2004). This is an unusual result if disk inclinations are random. It also creates a new set of problems when these objects are interpreted as almost face-on disks, because that often conflicts with outer disk inclinations derived from other imaging observations (*Hubble Space Telescope* [*HST*], radio). This result is difficult to accommodate in disk-only models but is easily explained by halo-embedded disks (V03).

In this paper we reexamine the DDN01 model and the theoretical approach behind it and identify some unresolved issues in its description of the rim emission. We employ exact radiative transfer calculations of the rim's brightness and show that the concept of a puffed-up rim requires some fine-tuning of the model parameters in order to produce enough flux to explain the observations (e.g., the dust must be perfectly gray).

Various independent observations indicate the existence of compact halos ($\sim$10 AU) around the disk inner regions (see V03 and references within), and we find that such halos readily explain the observed near-IR excess as well. Furthermore, the halos also resolve the puzzling relationship noted by Monnier & Millan-Gabet (2002) between luminosity and the interferometric inner radii of disks.

2. EMISSION FROM THE INNER WALL

A distinct feature of the near-IR bump is its anomalously high flux F_λ as compared with the stellar emission. To quantify this effect we introduce the flux ratio $F_{2\,\mu\mathrm{m}}/F_{1\,\mu\mathrm{m}}$ as a measure of the strength of the near-IR bump; this ratio increases when the prominence of the bump becomes larger. These wavelengths are chosen because the 2 μm flux is dominated by the dust, while the 1 μm flux is dominated by the star.

Figure 1 summarizes the observed values of the $F_{2\,\mu\mathrm{m}}/F_{1\,\mu\mathrm{m}}$ flux ratio for a sample of well-observed stars, with data compiled from the following references: Low (1970), Gillett & Stein (1971), Strom et al. (1972, 1989), Allen (1973), Cohen (1973a, 1973b, 1973c, 1975, 1980), Glass & Penston (1974), Cohen & Schwartz (1976), Kolotilov et al. (1977), Bouchet & Swings (1982), Lorenzetti et al. (1983), Tjin A Djie et al. (1984), Kilkenny et al. (1985), Thé et al. (1985), Olnon et al. (1986), Berrilli et al. (1987, 1992), Hu et al. (1989), Lawrence et al. (1990), Fouqué et al. (1992), Hutchinson et al. (1994), Li et al. (1994), Prusti et al. (1994), Sylvester et al. (1996), Garcia-Lario et al. (1997), Malfait et al. (1998), Herbst & Shevchenko (1999), van den Ancker et al. (2000), de Winter et al. (2001), and A. S. Miroshnichenko (2005, private communication).

Dust extinction at 1 μm is larger than at 2 μm and could enhance the observed strength of the near-IR bump by $\sim$20% for $A_V = 1$, and therefore only objects with $A_V \lesssim 1$ were considered. Since the reddening correction is negligible, the uncorrected data displayed in the figure represent the true range of near-IR bump strength in Herbig Ae stars. The underlying stars of all objects have temperatures of about 10,000 K, which gives $F_{2\,\mu\mathrm{m}}/F_{1\,\mu\mathrm{m}} = 0.09$. Yet in all objects this ratio exceeds 0.25, reflecting a large near-IR excess from hot dust emission (Hillenbrand et al. 1992). The luminosity of each object is displayed together with its name in Figure 1, and it ranges from $\sim$5 to $\sim$80 $L_\odot$. Luminosity does not show any correlation with the near-IR bump strength, reaffirming our conclusion that these data can be used as a general description of the near-IR bump strength in Herbig Ae stars.

2.1. *General Description of the Rim Emission*

At the inner rim, gas that is typically part of the disk cold interior becomes directly exposed to the stellar radiation and expands to higher scale heights. According to DDN01, emission from such a puffed-up rim can explain the near-IR bump in the spectrum of Herbig Ae/Be stars. The rim geometry is sketched in Figure 2. The rim is modeled as a cylinder of radius R_{rim} and height $2H_{\mathrm{rim}}$ centered on the star. The basic assumption of this model is that the rim is optically thick in the near-IR and shorter wavelengths. This maximizes the rim energy output.

The original DDN01 model (Dullemond et al. 2001) successfully explained the data, but it was based on an approximate treatment of the rim height and emission. More realistic models were calculated by the authors of the DDN01 model in their subsequent work. Dullemond (2002) used a two-dimensional radiative transfer model for gray dust combined with the hydrostatic equilibrium. The obtained near-IR bump strength is shown in Figure 1 (*solid line*). The maximum strength is still too low to explain all the data, but it can accommodate the majority of observed near-IR bump strengths.

A dramatic reduction of the DDN01 model efficacy happens when a mixture of small and big grains is introduced. Dullemond & Dominik (2004, hereafter DD04) combined 2 mm (big, gray grains) and 0.1 μm (small) grains in various ratios and performed two-dimensional radiative transfer calculations coupled to the equation of vertical hydrostatics and dust settling. The model fails to explain the data even when 99.999% of the dust mass is in big grains (see Fig. 1). The behavior suggested by this result is unexpected; a decrease in the small grain population leaves more gray dust grains in the mix, which should move the whole solution closer to the gray dust result of Dullemond (2002).

A closer inspection of obtained results shows that the temperature of big grains in such a multigrain mixture is lower than in the pure gray model. In a mixture, both small and big grains absorb a fraction of the local energy density and participate in providing the local diffuse heating. But, as shown in the next section (see also eq. [A8] in Appendix A), small grains are a very inefficient source of local diffuse heating, resulting in less efficient heating of the big grains than in the pure gray model. With such a temperature decrease, the vertical hydrostatic equilibrium cannot produce disk puffing comparable to the gray model. While in the gray model the puffed-up disk rim height is close to $H_{\mathrm{rim}}/R_{\mathrm{rim}} = 0.2$, multigrain models have only $H_{\mathrm{rim}}/R_{\mathrm{rim}} < 0.15$. Since the observed rim emission scales with rim height, this is the major reason behind the failure of the multigrain models to explain the data. Of the models presented, the one with the lowest fraction of small grains yields the largest discrepancy because it suffers the largest reduction in the small grain contribution to gas heating and rim puffing, while still having enough small grains to suppress heating of the big grains. In quantifying this effect, the mass ratio between big and small grains that DD04 used is not the most illustrative choice. A more appropriate quantity would be the "equivalent" grain size of the grain mixture. In the case of two grain populations with sizes a_{big} and a_{small} and fractional number densities X_{big} and X_{small} (such that $X_{\mathrm{big}} + X_{\mathrm{small}} = 1$), the average grain size obeys

$$\langle a^2 \rangle = X_{\mathrm{big}} a_{\mathrm{big}}^2 + X_{\mathrm{small}} a_{\mathrm{small}}^2. \quad (1)$$

The number fractions can be deduced from the reported parameters of the DD04 models: fixed inner and outer disk radius, fixed total disk mass, and total dust mass in big and small grains. The model with 99.999% of the dust mass in big grains has only $X_{\mathrm{big}} = 1.25 \times 10^{-8}$, and $X_{\mathrm{small}} \sim 1$, yielding $\langle a^2 \rangle^{1/2} \sim 0.25$ μm.

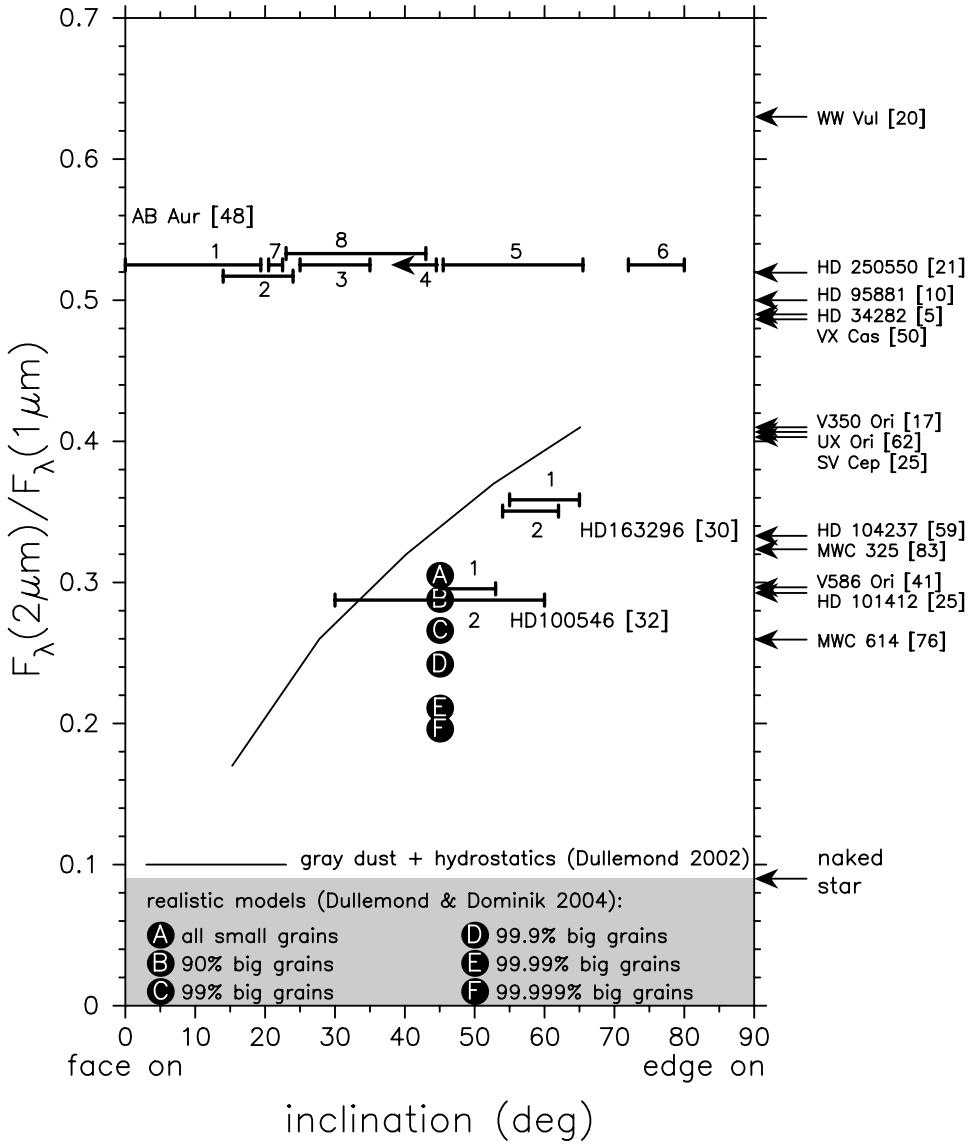

FIG. 1.—Strength of near-IR bump in Herbig Ae stars. The "naked star" arrow on the right axis marks the strength for a 10,000 K blackbody spectrum. Other arrows indicate the data (see § 2 for references) for systems with unknown disk inclination angles. These angles were estimated for three stars, as indicated. HD 163296: (1) Grady et al. (2000), (2) Mannings & Sargent (1997); HD 100546: (1) Grady et al. (2001); Augereau et al. (2001), (2) Liu et al. (2003); AB Aur: (1) Eisner et al. (2004, 2003), (2) Semenov et al. (2005), (3) Fukagawa et al. (2004), (4) Grady et al. (1999), (5) Liu et al. (2005), (6) Mannings & Sargent (1997), (7) Corder et al. (2005), (8) Piétu et al. (2005). Stellar luminosities in units of $L_\odot$ are indicated together with the stellar name. The solid line is a two-dimensional radiative transfer model of a puffed-up gray dust wall by Dullemond (2002). The filled circles with letters (realistic models, inclination $i = 45^\circ$) are two-dimensional radiative transfer models by Dullemond & Dominik (2004) that include a mixture of big and small dust grains. The rim height in all these models is calculated directly from the equation of vertical hydrostatics. While the gray dust model can explain the majority of data, the realistic models of puffed up rim fail to explain the data even when 99.999% of dust mass is in big (gray) grains.

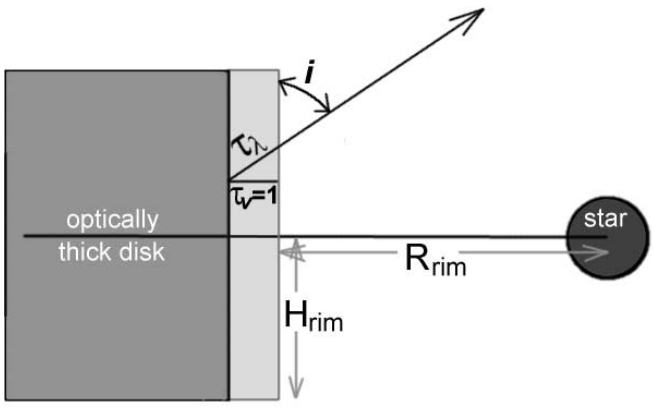

FIG. 2.—Sketch of the puffed up inner disk wall (see §§ 2.1 and 2.2 for details).

This grain size is too small to be considered equivalent to the gray dust model.

It is important to note that this equivalent grain is just an indicator of the overall solution and *cannot* be used as a general replacement (average or synthetic) grain for the radiative transfer calculation. As already shown by Wolf (2003), the approximation of an averaged single grain as a replacement for a dust mixture breaks down at the surface of a dust cloud (or in this case the rim surface). A more detailed study of multigrain disk models will be presented in a separate publication, while in the next sections we explore the limits of possible DDN01 model applicability in the context of single dust grains.

2.2. *Approximate Solution for the Rim Emission*

We denote with R_* and T_* the stellar radius and temperature, respectively. At distance d and direction i where the star is free of

rim obscuration (see Fig. 2), the overall observed flux at wavelength λ is $(R_*/d)^2\pi B_\lambda(T_*) + F_\lambda^{\rm rim}(i)$. If $I_\lambda^{\rm rim}(i)$ is the rim surface brightness in the observer's direction, then

$$F_\lambda^{\rm rim}(i) = \frac{1}{d^2} I_\lambda^{\rm rim}(i) 4 H_{\rm rim} R_{\rm rim} \sin i. \quad (2)$$

Here the cylindrical visible surface is replaced with a flat rectangle. This approximation maximizes the flux since curvature decreases the projected area of portions of the visible surface, reducing the observed flux. We also assume that the stellar illumination is perpendicular to all portions of the rim. This too maximizes the observed flux.

The observed rim flux in equation (2) is determined by the rim height, surface brightness and radius. Our two-dimensional radiative transfer calculations, described in § 2.3, confirm that the rim emission is indeed proportional to the rim height; therefore, we maximize the rim emission in this study by using $H_{\rm rim} = 0.2R_{\rm rim}$, the maximum height allowed before the rim starts to shadow large portions of the disk (DDN01). The solution for any other rim height can be derived from our models by a simple scaling of the rim emission.

The surface brightness of a gray dust rim can be approximated with $B_\lambda(T_{\rm rim})$, where $T_{\rm rim}$ is the dust sublimation temperature. The description of a nongray surface must take into account the spectral variation of optical depth of the emitting optically thin surface layer. This was done by Chiang & Goldreich (1997). According to their model, the surface layer vertical optical thickness is unity in the visual (a characteristic wavelength of the stellar radiation absorption), $\tau_V = 1$, and therefore at all other wavelengths it is $\tau_\lambda = \sigma_\lambda^{\rm abs}/\sigma_V^{\rm abs} \equiv q_\lambda$. The rim emits in the near-IR where $q_\lambda < 1$ (the dust near-IR opacity is smaller than in the visual), thus the surface layer is optically thin at these wavelengths and its emission is reduced accordingly. Therefore, the rim surface brightness becomes $\simeq q_\lambda B_\lambda(T_{\rm rim})/\sin i$ and the observed rim flux is

$$F_\lambda \simeq \frac{4}{d^2} B_\lambda(T_{\rm rim}) \frac{H_{\rm rim}}{R_{\rm rim}} R_{\rm rim}^2 \times \begin{cases} q_\lambda & \text{nongray dust} \\ \sin i & \text{gray dust} \end{cases} \quad (3)$$

This result shows that *a nongray rim creates a smaller IR excess than a gray opacity rim*. In addition, *nongray opacity removes the angle dependence from the rim emission* (we expect this approximation to break down at very small inclination angles, where $q_\lambda \sim \sin i$).

The rim radius is derived from radiative equilibrium, which gives (e.g., Ivezić & Elitzur 1997)

$$R_{\rm rim} = \frac{1}{2} R_* \left(\frac{T_*}{T_{\rm rim}}\right)^2 \left[\frac{\bar\sigma(T_*)}{\bar\sigma(T_{\rm rim})} \psi \left(1 + \frac{H_{\rm rim}}{R_{\rm rim}}\right)\right]^{1/2}. \quad (4)$$

Here $\bar\sigma(T)$ is the Planck average of $\sigma_\lambda^{\rm abs}$ at temperature T, ψ describes the correction for diffuse heating from the rim interior,[1] and $1 + H_{\rm rim}/R_{\rm rim}$ is a correction (described by DDN01) for self-irradiation from the other side of the rim. In Appendix A we derive an approximate solution, which shows that gray dust, with $\bar\sigma(T_*)/\bar\sigma(T_{\rm rim}) = 1$, has $\psi \sim 4$ and that nongray dust, with $\bar\sigma(T_*)/\bar\sigma(T_{\rm rim}) > 1$, has $\psi \sim 1$. Note that for gray dust this makes equation (4) identical to the original DDN01 expression (their eq. [14]). The approximate near-IR bump strength is given in equation (A10), yielding

$$\frac{F_{2\,\mu{\rm m}}}{F_{1\,\mu{\rm m}}} \sim \begin{cases} 0.23 & \text{nongray dust} \\ 0.09 + 0.52 \sin i & \text{gray dust} \end{cases} \quad (5)$$

for $T_* = 10{,}000$ K, $T_{\rm rim} = 1500$ K, and $H_{\rm rim}/R_{\rm rim} = 0.2$. A comparison of this result with the data in Figure 1 shows that the near-IR bump of nongray dust is too small to explain the observations. Therefore, interpretation of the near-IR bump in Herbig Ae stars with inner disk puffing places a strong constraint on dust evolution in this region. The dust must grow to a size greatly exceeding the initial interstellar size distribution, and small grains must be depleted to such a large extent that the inner disk opacity can be considered gray. In the next subsection we employ exact two-dimensional radiative transfer code to obtain accurate values for ψ and place more precise constrains on the DDN01 model.

2.3. *Exact Models for Single-Size Grains*

To examine the validity of conclusions based on our approximate solution, we performed full two-dimensional radiative transfer calculations for an optically thick torus centered on a 10,000 K star. The torus cross section is sketched in Figure 2; it is a square with side length of $2H_{\rm rim}$, where $H_{\rm rim} = 0.2R_{\rm rim}$. This configuration is the same as that described by DDN01, where the puffed-up disk rim is a cylindrical surface directly exposed to stellar radiation, while the rest of the inner disk is in its shadow. The dust has a sublimation temperature $T_{\rm sub} = 1500$ K and constant density everywhere in the torus, with horizontal and vertical optical depths $\tau_V = 10{,}000$ in the visual. Different density structures do not change our results as long as the $\tau_V = 1$ layer on the illuminated surface is geometrically much smaller than $H_{\rm rim}$.

Radiative transfer modeling was conducted with our code LELUYA[2] that works with axially symmetric dust configurations. It solves the integral equation of the formal solution of radiative transfer, including dust scattering, absorption, and thermal emission. The solution is based on a long-characteristics approach to the direct method of solving the matrix version of the integral equation (Kurucz 1969).

The results are shown in Figure 3 together with the original DDN01 solution (*dashed line*). Our two-dimensional model results for gray dust without scattering (*solid line*) are very close to the Dullemond (2002) results, shown in Figure 1, which also included vertical hydrostatics equilibrium. This model has $\psi = 4$. Its rim radius ($49R_*$) and flux are essentially the same as the original DDN01 model, confirming that a puffed-up rim of gray dust is capable of explaining the near-IR bump.

Since realistic dust is not gray at all wavelengths, we calculated models for silicate dust with different grain radii, employing optical constants from Dorschner et al. (1995) ($x = 0.4$ olivine). Figure 3 shows results for three representative grain radii, with the corresponding rim properties summarized in Table 1. Our model results for 0.1 μm grains are almost identical to the Dullemond (2002) results for purely small grains (see Fig. 1). As is evident from Figure 3, the model can explain the data when the grain radii are 2 and 0.5 μm, but it starts to fail as a general explanation of the near-IR bump when the grain radius drops below $\sim$0.1 μm.

A decrease in grain size has two opposing effects on the rim flux. On one hand, the ratio $\bar\sigma(T_*)/\bar\sigma(T_{\rm sub})$ is increasing, leading to a larger rim radius and emitting area and thus enhancing the

[1] Note that Ivezić & Elitzur (1997) used $\Psi = [\bar\sigma(T_*)/\bar\sigma(T_{\rm rim})]\psi$.

[2] See http://www.leluya.org.

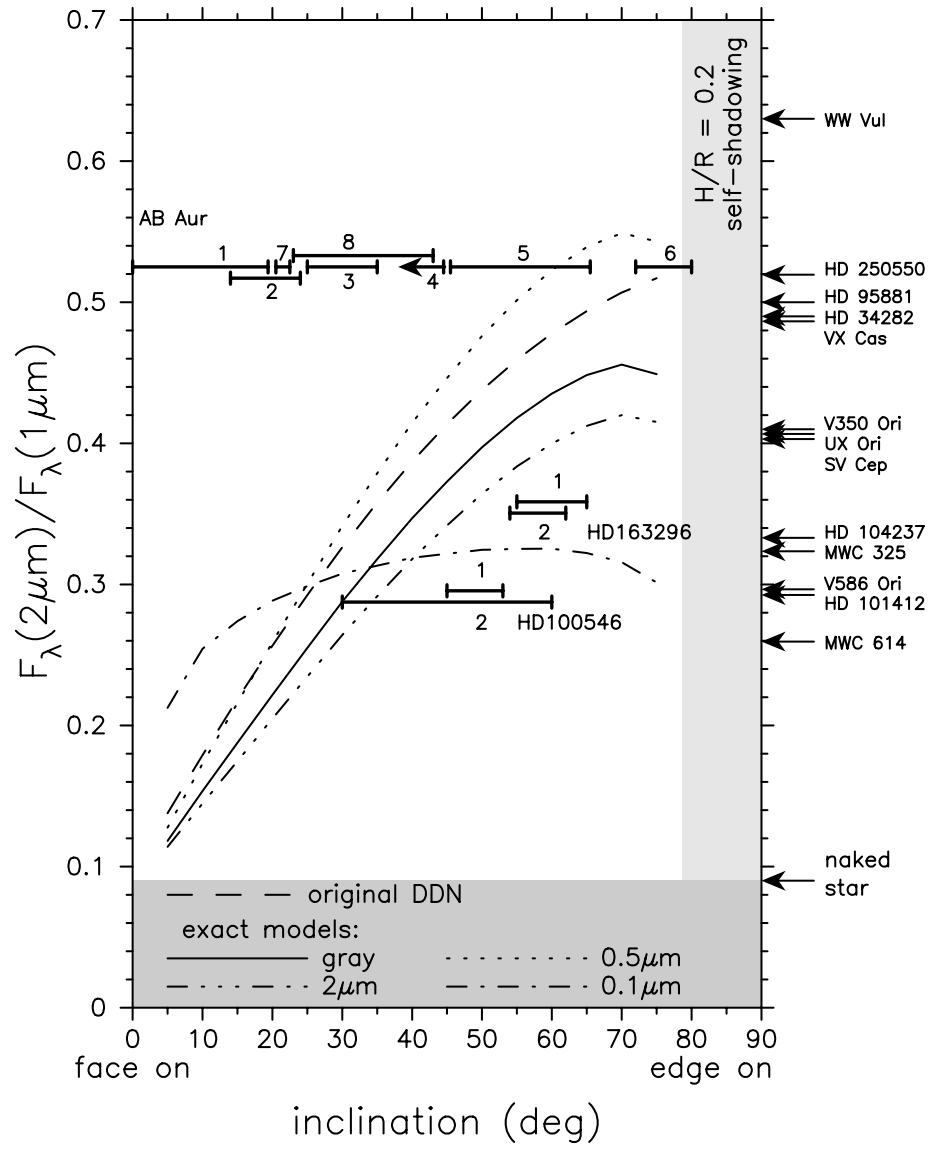

FIG. 3.—Same as Fig. 1, but for single-size grain models with $H_{\rm rim} = 0.2R_{\rm rim}$. The shaded areas are regions without flux contribution from the rim, because of either the absence of dust or rim self-shadowing. The dashed line is the original DDN01 model (Dullemond et al. 2001); all other lines show the results of exact two-dimensional radiative transfer calculations (see § 2.3).

rim emission. On the other, the rim surface brightness is declining because q_λ is decreasing, reducing the rim emission. The net result is that maximum rim emission occurs at grain radius of $\sim$0.5 μm, which, as is evident from Figure 4, corresponds to the transition between gray and nongray opacity in the near-IR region. This is predominantly a grain size effect; the dust chemistry introduces only second order corrections.

When the grain radius drops below 0.5 μm the dust opacity becomes nongray in the near-IR and the puffed-up rim model begins to fail. The flux of the 0.1 μm grain model, which is almost

TABLE 1
THE EXACT SINGLE-GRAIN DDN01 MODEL RESULTS

Grain Radius	$R_{\rm rim}/R_*$	$\tilde{\sigma}(T_*)/\tilde{\sigma}(T_{\rm sub})$	ψ	$q(2\ \mu{\rm m})$
Gray.....	49	1.0	4.0	1.00
2 μm.....	52	1.3	3.6	0.99
0.5 μm.....	68	3.6	2.3	0.45
0.1 μm.....	150	28	1.3	0.10

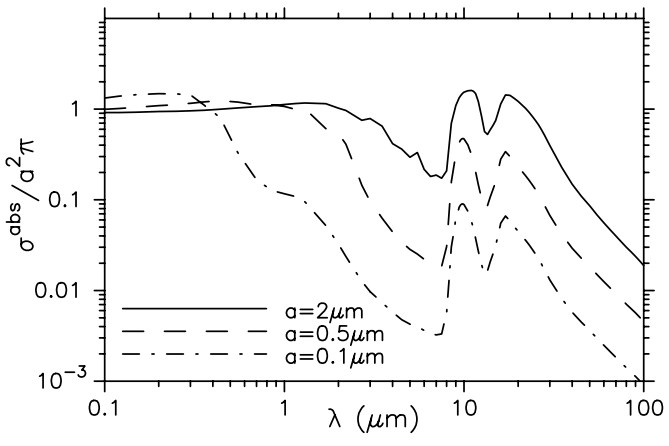

FIG. 4.—Dust absorption cross sections for the three grain radii used in the exact radiative transfer calculations shown in Fig. 3.

angle independent, as predicted by equation (A10), can reproduce only the weakest near-IR bumps. Therefore the DDN01 model can explain the near-IR bump in Herbig Ae stars only when *both* of the following conditions are met:

1. the rim dust opacity is gray in the near-IR (grain radius $\gtrsim 0.5\mu$m), and
2. the disk is puffed to a height $H_{\rm rim}/R_{\rm rim} \gtrsim 0.15$.

Figure 1 shows that for these conditions to be satisfied, the DDN01 model requires the complete absence of small grains in the disk inner region. Therefore, for this model to work, the rim dust must undergo substantial growth that also fully depletes the population of small grains. At the same time, this process cannot be so extreme in the rest of the disk because the mid-IR spectrum of Herbig Ae stars displays the dust features of small grain emission (van Boekel et al. 2005).

3. THE NEAR-IR BUMP AND IMAGING EXPLAINED WITH A DUSTY HALO

A dusty halo around the disk inner regions ($\sim$10 AU) has been invoked to explain polarimetric measurements (Yudin 2000) and correlations between variabilities in the optical and near-IR (Eiroa et al. 2002). Such small regions are not yet accessible to direct imaging but have been resolved in near-IR interferometry by Millan-Gabet et al. (2001), who also favor the halo geometry, although the interpretation of these visibility data is still model dependent. Direct imaging is currently available only for larger scales, and these observations have revealed larger halos ($\gtrsim$100 AU) around some objects (V03). The relation between the inner and outer halos, whether they are simply the inner and outer regions of the same circumstellar component, remains an open question. However, at the phenomenological level this issue is not relevant because the two can be treated as separate circumstellar components if both are optically thin. The inner halo is then radiatively decoupled from the cooler outer halo, simplifying the study of inner halos.

Here we explore the contribution of the inner halo to the near-IR emission. The halo precise geometry is not particularly important. It could be elongated, clumpy or inhomogeneous, but as long as it is optically thin it can be approximated with spherical geometry. The reason is that the temperature of optically thin dust is dominated by the stellar heating, resulting in spherically symmetric isotherms and circularly symmetric images at wavelengths where the dust thermal emission dominates over scattering (V03). Optically thin halos are also transparent to the disk emission, and we can ignore the disk effect on the halo. The exact image shape ultimately depends on detailed dust density and grain properties, telescope resolution and sensitivity, observational wavelength, and the intrinsic ratio between the disk and halo surface brightness. Various observations of R Mon vividly illustrate these effects (see Weigelt et al. 2002).

If the halo optical depth at visual wavelengths τ_V is larger than $\frac{1}{4}H/R$, where H/R is the disk flaring at the halo outer radius, then the halo dominates the SED coming from the dust within radius R around the star (see V03 for details). At near-IR wavelengths, this condition is satisfied for the halo optical depths of interest here ($\tau_V \gtrsim 0.1$).

3.1. *Theoretical Examples*

Our models consist of a star surrounded by a spherical halo with radial density profile $\eta \propto r^{-p}$. The halo extends from inner radius $R_{\rm in}$, set by the dust sublimation temperature $T_{\rm sub}$, to outer radius $R_{\rm out}$.

The dust chemistry is $x = 0.4$ olivine from Dorschner et al. (1995), with grain size distribution $n(a) \propto a^{-q}$ between the minimum grain radius $a_{\rm min}$ and maximum $a_{\rm max}$. We use $q = 2$ and $a_{\rm min} = 0.01$ μm and vary $a_{\rm max}$. The radial optical depth of the halo is specified at $\lambda = 0.55$ μm as τ_V. The radiative transfer problem is solved with the code DUSTY (Ivezić et al. 1999), which takes advantage of the scaling properties of the radiative transfer problem for dust absorption, emission, and scattering (Ivezić & Elitzur 1997).

Figures 5 and 6 show some SED examples for dusty halos around 10,500 and 5000 K stars, representative of Herbig Ae and T Tauri stars, respectively. The stellar spectrum is taken from Kurucz models. In addition to the strength parameter $F_{2\ \mu{\rm m}}/F_{1\ \mu{\rm m}}$, the flux ratio $F_{4\ \mu{\rm m}}/F_{2\ \mu{\rm m}}$ can be used to characterize the near-IR bump shape. Both the strength and shape parameters are influenced by changes in the dust sublimation temperature, maximum grain size, halo outer radius, and optical depth. Comparison of the data with halo model results for the strength and shape parameters is shown in Figure 7 for the same objects as in Figure 3. Models for $p = 1$ and $p = 2$ halos around a 10,500 K star are dispersed all over the diagram. Arrows show how the model results move in the diagram as the model parameters are varied, indicating that various degeneracies are possible. The observed levels of bump strength and shape are readily reproduced with plausible values of the model parameters.

We briefly summarize the effect of various halo parameters on the strength and shape of the near-IR bump.

Optical depth.—A larger optical depth results in a stronger near-IR bump. This reflects the dependence of flux on the total mass of emitting dust (eqs. [A7] and [A12] in V03). The dust sublimation radius $R_{\rm in}$ is only slightly affected, as expected in the optically thin limit, at which the diffuse radiation is negligible.

Grain size.—Larger grains shift the near-IR bump toward longer wavelengths and make it appear more flat. With increased grain size the opacity becomes more similar to gray dust, resulting in an $r^{-0.5}$ temperature profile, since the geometrical dilution of stellar heating is the only cause of temperature variation. Smaller grain sizes create steeper radial temperature profiles. Therefore, for a given density profile smaller grains emit relatively more radiation at shorter wavelengths than larger grains. In practice, grain sizes come in mixtures and sublimate at different radial distances, greatly adding to the complexity of the problem. The SED models are therefore prone to various model degeneracies.

Sublimation temperature.—With a higher dust sublimation temperature, the near-IR bump shifts to shorter wavelengths, reflecting the shift of the emission peak.

Outer radius.—The halo size can affect the near-IR bump in two ways. On the one hand, reducing the outer radius while keeping the dust distribution fixed reduces also the total optical depth. The near-IR bump then starts to decrease when the dust removal reaches the near-IR emission regions at radial distance $\sim 10R_{\rm in}$ (temperatures $\gtrsim$500 K). On the other, reducing the outer radius at a fixed halo optical depth is equivalent to redistributing the dust within the halo. The bump then becomes stronger as the outer radius is reduced because more dust is shifted toward smaller radii and higher temperatures.

Stellar temperature.—As its temperature decreases, the emission from the star starts to blend with that from the halo, and the near-IR bump disappears. Only a careful analysis can then separate the stellar from the diffuse flux in the near-IR and reveal the bump. For comparison with T Tau stars, Figure 7 shows also 5000 K models (marked with T). In spite of the large variations in halo parameters, these models display only a limited range of bump strengths and shapes close to the naked star values. This

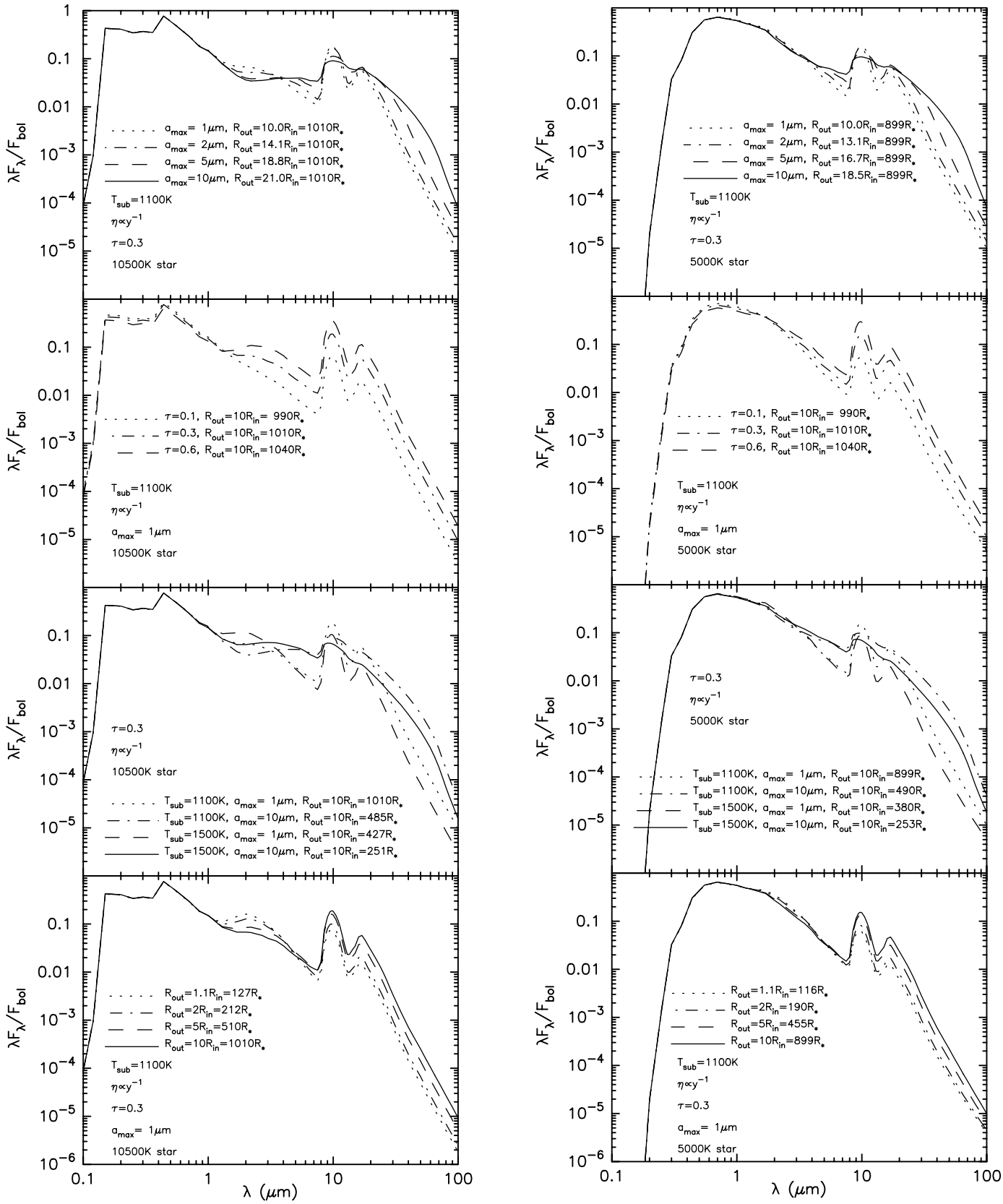

FIG. 5.—SED variation with the parameters of small spherical halos around stars with 10,500 and 5000 K (Kurucz stellar models). The radial density profile is $\eta \propto y^{-1}$. The dust chemistry is $x = 0.4$ olivine from Dorschner et al. (1995). The grain size distribution is $n(a) \propto a^{-2}$ between minimum grain radius 0.01 μm and maximum $a_{\max}$, as marked. The other varied parameters are the dust sublimation temperature $T_{\rm sub}$, which sets the halo inner radius $R_{\rm in}$, the halo outer radius $R_{\rm out}$ and its optical depth at visual τ. Note the variation of $R_{\rm in}$ among models, especially when $a_{\max}$ is increased.

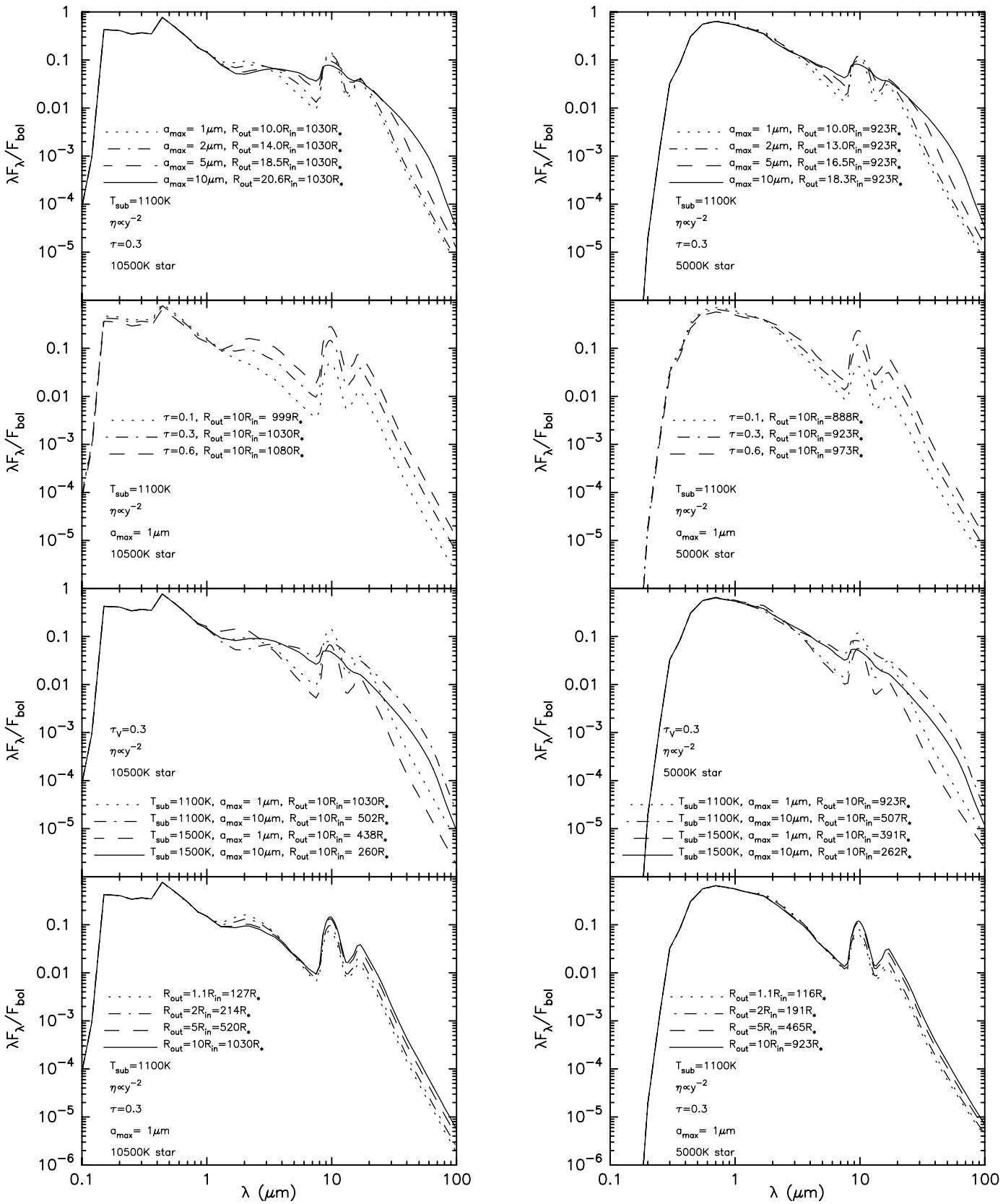

FIG. 6.—Same as Fig. 5, except that $\eta \propto y^{-2}$.

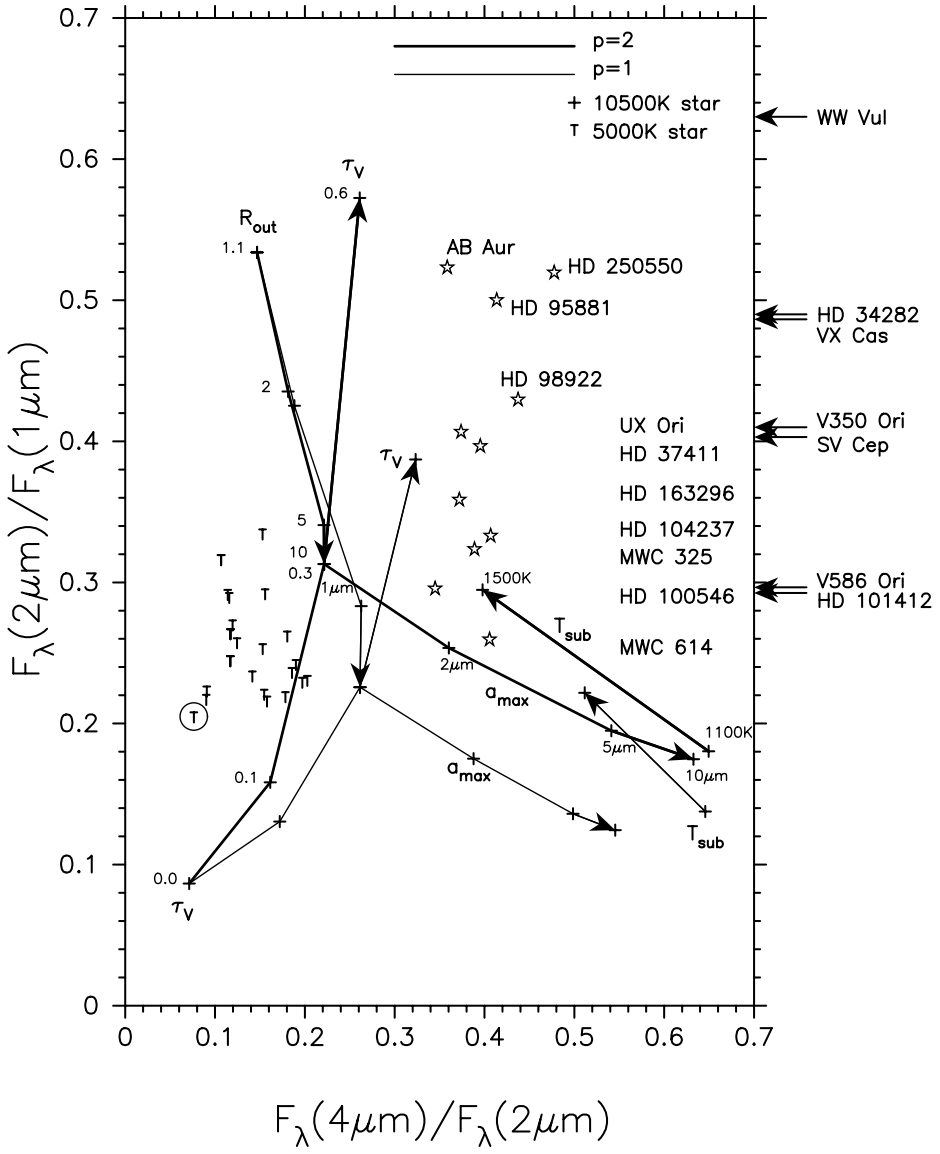

FIG. 7.—Diagram of the strength (*vertical axis*) vs. shape (*horizontal axis*) of the near-IR bump. Data are for the same sources as in Fig. 1. Objects with enough data to determine the bump shape are marked with stars; otherwise, only their bump strengths are marked with arrows on the right. Theoretical results for the halo models presented in Figs. 5 and 6 are marked with crosses for halos around a 10,500 K star and with T for halos around a 5000 K star (the location of this naked star is marked with encircled T). Model results for the 10,500 K case are connected with arrowed lines that indicate their path in the diagram when only one parameter is varied, as marked. Thick lines correspond to $p = 2$ halos, and thin lines to $p = 1$.

explains why the near-IR bump was not originally recognized in T Tau stars, while it was easily detected in Herbig Ae/Be stars.

3.2. *Observational Examples*

We show three examples that illustrate different circumstellar dust configurations: AB Aur, HD 100546, and HD 163296. *HST* imaging suggests that AB Aur and HD 100546 have large halos at radii $\gtrsim 1''$, while HD 163296 shows only a disk (Grady et al. 2003). Irrespective of the existence of a large halo, all three objects show a near-IR bump, with the strongest bump in AB Aur. Since the focus of this study is the near-IR bump, the large-scale halos are irrelevant here, and we only consider a small halo within $\sim$10 AU around the star.

Our fits to the data are shown in Figure 8, with the model parameters listed in Table 2. The halo outer radius is 10 times the dust sublimation radius in all models. Since our focus is the near-IR bump, our model consists only of the star and the inner halo, and only data at wavelengths shorter then 6 μm were employed in the fitting. The derived model parameters are not unique, since various degeneracies exist in model results for the near-IR flux (see § 3.1). For example, the "hot component" in the Bouwman et al. (2000) models can be interpreted as a small-scale halo with dust properties different from those in our study.

3.2.1. *AB Aur*

The emission from AB Aur has been resolved at various wavelengths and interpreted as a disk with vastly different estimates for the inclination angle, as listed in Table 3. Such a disparity is expected in halo-embedded disks (see Fig. 7 in V03) because, as noted by Miroshnichenko et al. (1999), the halo dominates the images at wavelengths extending to $\sim$100 μm or so, and the disk emerges only at longer wavelengths. Interpretation of molecular line images, too, must be done carefully to avoid confusion between the halo and disk contributions.

A general conclusion about the AB Aur inner halo is that it must have a radial density profile between $1/r$ and $1/r^2$; this

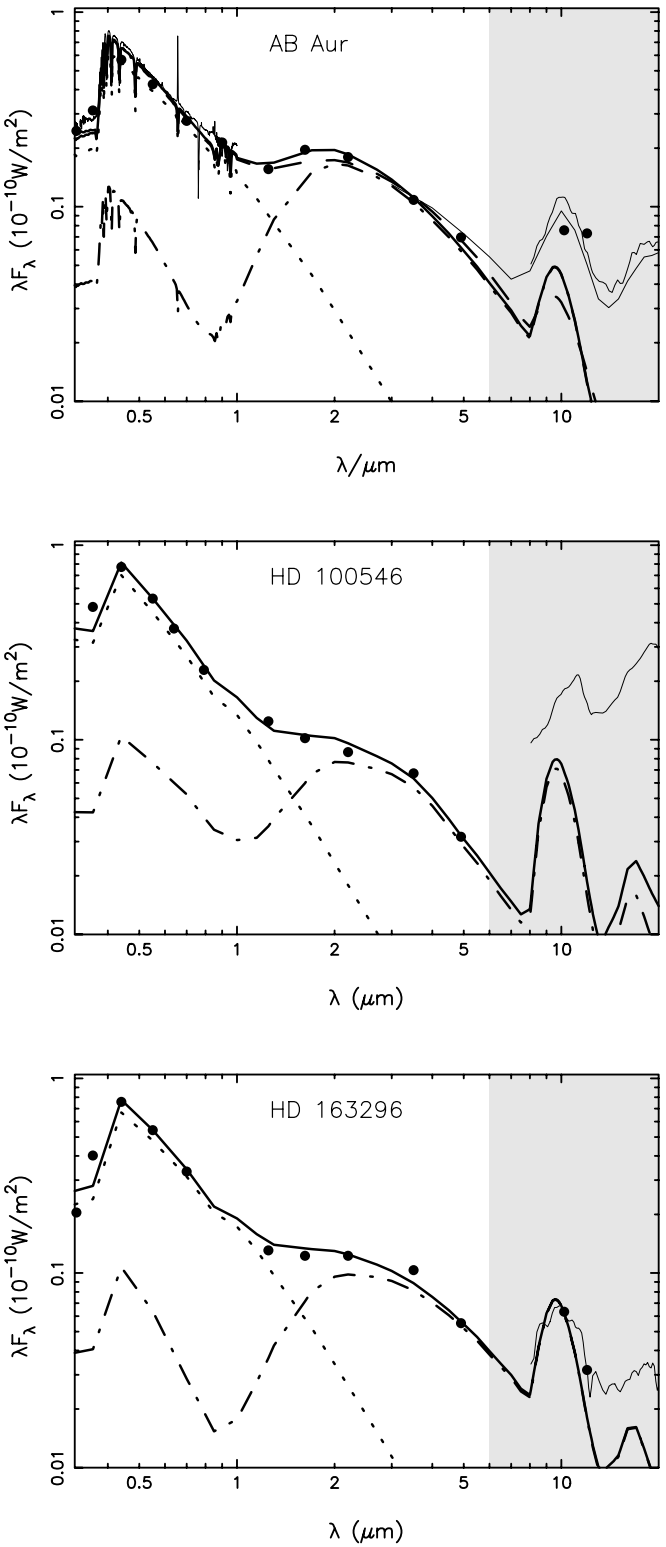

FIG. 8.—Models for the near-IR bumps in AB Aur, HD 100546, and HD 163296. Points and thin solid lines are the data (see § 2). Measurement uncertainties in the near-IR are comparable to the symbol sizes. Thick solid lines are the models, comprised of the stellar component (*dotted lines*) and a halo contribution (*dash-dotted lines*); see text and Table 2 for model details. In the case of AB Aur, the thick dashed line is the second model listed in Table 2. Only data at wavelengths shorter then 6 μm were employed in the fits, since in this study we consider only the inner halo responsible for the near-IR bump. Longer wavelengths (*gray area*) are displayed to show the halo contribution to the mid-IR features; in HD 163296 this contribution suffices to explain the observed 10 μm feature.

differs from the outer halo, which has a $1/r$ density profile, as deduced from the $1/r^2$ radial brightness profile of the *HST* image (Grady et al. 1999; see also eq. [A10] in V03). Conclusions regarding the properties of the dust grains in the inner halo are less firm. Near-IR interferometry suggests the presence of dust close to the star, implying large grains that can survive at small distances. An example of a big-grains model for AB Aur is shown in Figure 8 (*thick dashed line*; see also Table 2). The grain size and chemistry might be subject to radial variations, as is indicated by comparison between the *HST* (Grady et al. 1999) and Subaru images (Fukagawa et al. 2004), further complicating the modeling.

3.2.2. *HD 100546*

The *HST* image of this source (Grady et al. 2001) shows a very tenuous large-scale nebulosity, whose low surface brightness implies an optical depth of only $\tau_V \sim 0.015$. This component of the dust distribution does not contribute significantly to the IR emission and can be ignored in the current analysis. The *HST* image, which is produced purely by scattered light, reveals also a prominent disk with inclination angle $49^\circ \pm 4^\circ$. Near-IR (Augereau et al. 2001) and mid-IR (Liu et al. 2003) imaging give similar results for the disk, even though the latter is produced purely by dust emission and the former contains a mixture of both scattering and emission. The *HST* brightness contours are symmetric, with the brightness declining as $1/r^3$. These are the signatures of scattering from the CG97 layer of a flat disk (see V03). However, for the CG97 model to be applicable, every point on the scattering surface, which extends to a distance of $\sim 10''$ from the star, must have a direct line of sight to the stellar surface. This is impossible in the case of a flat disk, since it would have to maintain a thickness smaller than the stellar radius for hundreds of astronomical units. Therefore, the only self-consistent explanation of the *HST* imaging is with an optically thin halo whose dimensions are unrelated to the stellar size. The *HST* image implies that the halo has a flattened geometrical shape, and its $1/r^3$ brightness profile implies that it has a $1/r^2$ radial density profile (V03). This flattened halo is outlined as region A in Figure 9. Since the halo dominates the imaging, the geometry of the optically thick disk structure, outlined as region B in the figure, remains unknown.

The *HST* imaging does not constrain the inner halo geometry at radii $\lesssim 10$ AU. The surface density must be reduced in that region because the near-IR bump in HD 100546 is significantly smaller than in AB Aur, even though otherwise the two stars are rather similar. Indeed, the fit to the near-IR bump yields a $1/r$ radial density profile (Fig. 8 and Table 2), shallower than in the region resolved by *HST*. The fit was further improved by an increased contribution from large grains ($a_{\max} = 0.5$ μm and $q = 2$) and a reduced fraction of carbon dust in the mix. Observations by Grady et al. (2005) show that a constant density profile, creating $1/r$ brightness profile, might be more appropriate in the region between 20 and 50 AU. We find that a constant density model could also fit the near-IR spectrum if the sublimation temperature were increased to 1700 K. All these results point toward large structural differences between the inner and outer regions of HD 100546.

3.2.3. *HD 163296*

The model properties of the inner halo in this source are very similar to AB Aur, except that a shallower density profile of $p = 1$ is preferred (see Table 2). A similar general conclusion is that the halo radial density profile is between $1/r$ and $1/r^2$, with uncertainties in the dust properties. Significantly, in this source the inner halo also fits the 10 μm feature all by itself (Fig. 8). No

TABLE 2
HALO MODEL PARAMETERS FOR THREE CASE STUDIES OF HERBIG AE STARS

Object (1)	T_* (K) (2)	A_V (K) (3)	T_{sub} (4)	τ_V (5)	η (6)	R_{in} (AU) (7)	F_{bol} (10^{-10} W m^{-2}) (8)	Grain Radius (μm) (9)	Carbon (%) (10)	Olivine (%) (11)
AB Aur	9750	0.35	1500	0.35	r^{-2}	0.78	0.9	$q = 3.5$, $a_{max} = 0.25$	40	60
AB Aur	9750	0.35	1800	0.35	r^{-2}	0.25	0.9	$q = 3.5$, $a_{max} = 5.0$	40	60
HD 100546	10,500	0.3	1500	0.35[a]	r^{-1}	0.45	0.8	$q = 2$, $a_{max} = 0.50$	10	90
HD 163296	9500	0.3	1500	0.25	r^{-1}	0.61	0.9	$q = 3.5$, $a_{max} = 0.25$	30	70

NOTES.—Col. (2): T_*, stellar temperature; col. (3): A_V, reddening toward the star by dust other than the inner halo; col. (4): T_{sub}, dust sublimation temperature; col. (5): τ_V, visual optical depth of the halo; col. (6): η, radial dust density profile of the halo; col. (7): R_{in}, halo inner radius determined from dust sublimation. The halo outer radius is $10R_{in}$. Col. (8): F_{bol}, total bolometric flux; col. (9): grain radius, dust size distribution a^{-q} between minimum $a_{min} = 0.005$ μm and maximum a_{max}. Cols. (10)–(11): Amorphous carbon properties are from Hanner (1988), and olivine from Dorschner et al. (1995) (with $x = 0.4$).

[a] HD 100546 is modeled with a flattened halo, which does not contribute to the circumstellar reddening because the dust is out of the line of sight toward the star (see Fig. 9).

other optically thin components are required for explaining the mid-IR dust features, and indeed none are observed. The *HST* image, which is incapable of resolving the inner halo, shows no evidence of a large-scale structure other than the disk, with an inclination of $60^\circ \pm 5^\circ$ (Grady et al. 2000), in agreement with $\sim 58^\circ$ derived from millimeter observation (Mannings & Sargent 1997). Another noteworthy feature of the *HST* image is a bipolar jet. The process responsible for jet formation could perhaps also lift up dust above the disk and create the small-scale halo responsible for the near-IR bump. Such a possible correlation between jets and the near-IR bump can be studied further when additional high-resolution data from a larger sample of objects become available.

3.3. *Size-Luminosity Correlation*

The milliarcsecond resolution reached in near-IR interferometry enables studies of the immediate environment of young stars, down to 0.1 AU (Malbet 2003). Unfortunately, current visibility data are not yet capable of reproducing the full two-dimensional image of an object, instead requiring a model of the geometry for their analysis. One simple and often used model of the circumstellar geometry is a flat dust ring of uniform surface brightness. This ad hoc model did not arise from some specific radiative transfer modeling but rather chosen as a simple approach to the visibility fitting procedure.

Fitting the visibility data of a number of objects with this ring model, Monnier & Millan-Gabet (2002) discovered that the size of the ring inner radius increased with the stellar luminosity L_*. This is the expected result when dust sublimation controls the size of the dustfree region around the star. Since radiative transfer is scale invariant (Ivezić & Elitzur 1997), inner radii of rings would be expected to scale as $L_*^{1/2}$ if their dust properties were the same. However, Monnier & Millan-Gabet (2002) do not find such a trend. Instead, at a fixed luminosity the derived radii vary by almost a factor of 10, which they refer to as scatter in the size-luminosity diagram. This scatter indicates either that the disk inner regions have vastly different properties, with the sublimation temperature varying from $\sim$1000 to $\sim$2000 K, or that the ring model is not a proper description of the actual dust distribution. Monnier & Millan-Gabet (2002) also noted that some highly luminous objects ($L_* \gtrsim 10^3\ L_\odot$) had smaller than expected inner ring radii, thus requiring even higher dust sublimation temperatures. New interferometric data by Monnier et al. (2005) slightly reduce the scatter in the ring-radius–luminosity relation, but the remaining scatter still implies a large range of sublimation temperatures, and very luminous objects still display abnormally small radii.

Instead of the ring model we have analyzed the interferometry results with the inner halo model, performing simultaneous fits of both the near-IR bump and visibility data. Preliminary results are shown in Figure 10. It is highly significant that there are no objects in the forbidden region below the indicated lower limits. The correlation of overall bolometric luminosity with inner radius is much tighter than in the ring model, the small remaining scatter arises from variation in halo optical depth and grain size. In contrast with the ring model, the sublimation temperature rarely differs from 1500 K (it is 1800 K in a couple of objects). The high-luminosity object MWC297, which was especially troubling in the Monnier & Millan-Gabet (2002) analysis, is now consistent with 1500 K sublimation temperature. It is striking how some of the objects that were highly scattered in the diagram by Monnier & Millan-Gabet (2002) now settle on the same $L_*^{1/2}$ size-luminosity relation (Fig. 10, *dotted line*), indicating similarities

TABLE 3
ESTIMATED DISK INCLINATION ANGLES FOR AB AUR

Wavelengths	Inclination (deg)	Source
Visual	$\lesssim 45$	Grady et al. (1999)
Near-IR.....	$\lesssim 30$	Eisner et al. (2003, 2004)
	30 ± 5	Fukagawa et al. (2004)
Mid-IR.....	55 ± 10	Liu et al. (2005)
Millimeter.....	17^{+6}_{-3}	Semenov et al. (2005)
	$21.5^{+0.4}_{-0.3}$	Corder et al. (2005)
	33 ± 10	Piétu et al. (2005)
	~ 76	Mannings & Sargent (1997)

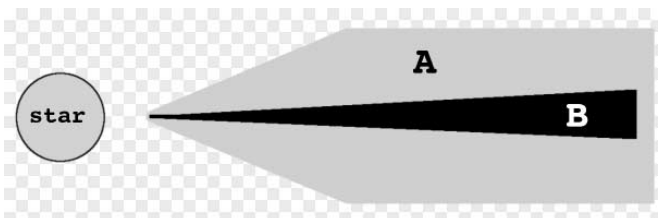

FIG. 9.—Sketch of the circumstellar geometry indicated by imaging observations of HD 100546 (Grady et al. 2001, 2005; see § 3.2.2). Region A is an optically thin dust layer, dominating the near-IR flux. The disk, marked with B, is cooler and does not affect the near-IR wavelengths. Both regions A and B are embedded in an optically thin dusty envelope, marked with checkered pattern, whose optical depth is so small that its contribution, too, to the near-IR flux is negligible.

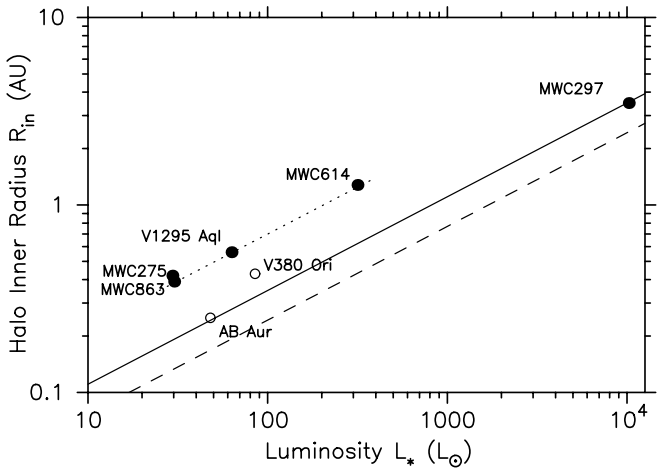

FIG. 10.—Size-luminosity diagram for the inner halo model. The sublimation radius R_{in} of each displayed object is determined from a simultaneous fit to its near-IR bump and visibility data. The filled circles mark objects with a dust sublimation temperature of 1500 K, the empty circles those with 1800 K. Lower limits on R_{in} are shown with the solid line for $T_{sub} = 1500$ K and the dashed line for $T_{sub} = 1800$ K; they correspond to halos of gray dust and zero optical depth. The dotted line connects a group of objects that follow closely the $R_{in} \propto L_*^{1/2}$ relation, indicating that their inner halos have similar optical depth and dust properties. The original version of this diagram, constructed from ring-model visibility analysis, produced a puzzling amount of scatter (see § 3.3) (Monnier & Millan-Gabet 2002). The inner halo model resolves the puzzle.

in the halo properties of all these stars, and in turn pointing toward a common physical mechanism of halo formation.

4. CONCLUSIONS

An examination of the puffed-up disk rim model (DDN01) shows that it has rather limited capabilities in explaining the near-IR bump of Herbig Ae/Be stars. The observed level of near-IR excess implies a certain emitting volume of optically thin puffed-up disk rim surface for given dust properties. The volume derived from the DDN01 model falls short of this observational limit, unless the disk is made of perfectly gray dust. The puffed-up rim produces enough near-IR flux *only* when the inner disk consists purely of dust grains larger than ~ 0.5 μm *and* the disk puffing reaches values of $H_{rim}/R_{rim} \gtrsim 0.15$. Models by Dullemond & Dominik (2004) show that even traces of small grains inhibit the disk puffing, eliminating the DDN01 model as a viable explanation of the near-IR bump. Since the 10 μm emission feature indicates the presence of small grains in the circumstellar dust, additional mechanisms must be invoked to remove all small grains from the inner disk and keep the DDN01 model viable.

From fits to the SED of a number of HAEBEs, Dominik et al. (2003) conclude that the infrared excess in these stars is produced by disks alone without the need for additional circumstellar components. This conclusion is invalidated by the mathematical proof that a fit to the SED cannot distinguish between the surface of a flared disk and an optically thin halo (V03). Fits to the SED alone are not a conclusive proof of a particular dust geometry.

We find that the optically thin dusty halos around the disk inner regions whose existence has been inferred in various observations readily explain the strength and shape of the near-IR bump. The halo is not limited by the disk properties. Hence, it can extend above the disk surface and accommodate the emitting optically thin dust volume required by the near-IR flux observations. The required halo is rather small, less than several astronomical units in size, and its optical depth in the visual is less than ~ 0.4. Despite its small optical depth, the halo dominates the near-IR spectrum and hides the disk near-IR signature. However, detailed properties of the halo, such as its exact shape, grain properties, or dust density profile, are not uniquely constrained by the SED, since different combinations of the parameters can produce the same flux. These degeneracies can be broken only with imaging capable of resolving the disk inner regions.

Inner halos not only explain the near-IR bump but also successfully resolve the puzzle presented by the relations between luminosities and near-IR interferometric sizes (Monnier & Millan-Gabet 2002). In addition to their near-IR emission, the halos contribute also to the mid-IR flux. HD 163296 is an extreme example where the halo in itself fully explains the mid-IR dust features without the need for additional extended components (Fig. 8). The absence of such components in the *HST* image of this source is another success of the inner halo model. In general though, the inner halo emission is not expected to dominate the mid-IR but still make a significant contribution that must be included in fits to the overall SED for reliable modelling of the rest of the circumstellar material. Recently, van Boekel et al. (2003) suggested that differences in the strength and shape of the mid-IR silicate feature in HAEBEs are evidence for dust settling in the disk. However, these differences could instead reflect halo evolution, with the most active stars showing the strongest mid-IR signature of the inner disk halo. High-resolution imaging is necessary for definite conclusions about the evolution either of the dust or the circumstellar disk. Such imaging will soon become available from the VLTI, which offers milliarcsecond resolution at near-IR.

We thank C. P. Dullemond, C. Dominik, and A. Natta for fruitful discussions on the physics of the DDN01 model. We also thank A. S. Miroshnichenko for help with the data compilation. D. V. thanks B. Draine and R. Rafikov for useful comments. Support by NSF grant PHY-0070928 (D. V.) is gratefully acknowledged. This work was also supported by National Computational Science Alliance (NCSA) under AST 04-0006 and utilized the NCSA's Xeon Linux Cluster. D. V. also thanks the Institute for Advanced Study (IAS) for time on their Linux cluster. T. J. acknowledges the hospitality and financial support of IAS during his visit to the institute. M. E. acknowledges partial support by NSF and NASA.

APPENDIX A

APPROXIMATE SOLUTION FOR THE RIM RADIUS

The observed emission from a puffed up inner disk depends on the rim radius, height, and surface brightness (see § 2.2). Deriving the rim radius requires a proper treatment of the rim temperature structure. As already noted by Dullemond (2002), in gray dust the diffuse radiation creates a temperature inversion—the dust temperature is maximum in the rim interior (that is, at $R > R_{rim}$), not on the rim surface. Here we derive an approximate solution for the dust temperature T_0 on the rim surface and the temperature T_1 inside the rim at depth $\tau_V \sim 1$ from the surface. The solution demonstrates the inversion effect for gray dust and shows that it does not exist in the nongray case.

A1. DUST TEMPERATURE T_0 ON THE RIM SURFACE

Consider a dust grain on the rim surface. It is heated by the stellar flux F_* and the diffuse flux $F_{\rm out}$ coming out from the rim interior. For large optical depths these two fluxes are balanced: $F_* = F_{\rm out}$. Stellar flux absorbed by the grain is $\sigma_V F_*$, where σ_V is the dust cross section in visual. Absorbed diffuse flux is $\sim 2\sigma_{\rm IR} F_{\rm out}$, where $\sigma_{\rm IR}$ is the cross section in the near-IR and the factor 2 accounts for absorption from 2π sr. The grain emits into 4π sr, so that the energy balance is

$$\sigma_V F_* + 2\sigma_{\rm IR} F_{\rm out} = 4\sigma_{\rm IR}\sigma_{\rm SB} T_0^4, \tag{A1}$$

where $\sigma_{\rm SB}$ is the Stefan-Boltzmann constant. Using $F_* = F_{\rm out}$, we get

$$\sigma_{\rm SB} T_0^4 = \frac{F_*}{4}\left(2 + \frac{\sigma_V}{\sigma_{\rm IR}}\right). \tag{A2}$$

A2. DUST TEMPERATURE T_1 at $\tau_V \sim 1$ FROM THE SURFACE

Now consider a dust grain at distance $\tau_V \sim 1$ from the surface into the rim. This grain is heated by the attenuated stellar flux $F_* \exp(-\tau_V) = F_* \exp(-1)$, by the diffuse flux from the surface dust between $\tau_V = 0$ and ~ 1, and by the diffuse flux from the rim interior. The absorbed stellar flux is $\sigma_V F_* \exp(-1)$. Diffuse contribution from the surface dust layer is $\sim 2\sigma_{\rm IR}\sigma_{\rm SB} T_0^4 \tau_{\rm IR}$, where $\tau_{\rm IR} \sim \sigma_{\rm IR}/\sigma_V$ is the infrared optical depth of this surface layer. Diffuse heating from the rim interior, described by temperature T_1, is $\sim 2\sigma_{\rm IR}\sigma_{\rm SB} T_1^4$. This is a good approximation for gray dust and an overestimate for nongray dust, where that temperature decreases rapidly with optical depth. The energy balance is

$$\sigma_V F_* \exp(-1) + 2\sigma_{\rm IR}\sigma_{\rm SB} T_0^4 \tau_{\rm IR} + 2\sigma_{\rm IR}\sigma_{\rm SB} T_1^4 = 4\sigma_{\rm IR}\sigma_{\rm SB} T_1^4. \tag{A3}$$

Using T_0 from equation (A2) we get the interior temperature

$$\sigma_{\rm SB} T_1^4 = \frac{F_*}{4}\left(2\frac{\sigma_{\rm IR}}{\sigma_V} + 1 + 2\frac{\sigma_V}{\sigma_{\rm IR}} e^{-1}\right). \tag{A4}$$

Note that the ratio T_0/T_1 depends only on $\sigma_{\rm IR}/\sigma_V$ and is independent of F_*.

A3. GRAY AND NONGRAY REGIMES

We consider two distinct opacity regimes: gray when $\sigma_{\rm IR}/\sigma_V \sim 1$ and nongray when $\sigma_{\rm IR}/\sigma_V \ll 1$. The ratio of the rim surface temperature T_0 and the interior temperature T_1 in these two regimes is

$$T_0/T_1 = 0.95, \tag{A5}$$

when $\sigma_{\rm IR}/\sigma_V = 1$ (gray dust), and

$$T_0/T_1 \sim 1.08, \tag{A6}$$

when $\sigma_{\rm IR}/\sigma_V \ll 1$ (nongray dust).

The gray opacity creates a temperature inversion with the temperature in the rim interior higher than on its surface. This inversion does not appear in nongray dust, for which the temperature decreases monotonically with distance from the rim surface. If the maximum dust temperature is 1500 K (sublimation temperature), then gray dust has $T_1 = 1500$ K and $T_0 \sim 1400$ K, while nongray dust has $T_0 = 1500$ K and $T_1 \lesssim 1400$ K.

These approximate expressions are in reasonable agreement with the results of exact two-dimensional radiative transfer calculations (see § 2.3), which yield $T_0 = 1387$ K and $T_1 = 1490$ K for gray dust and $T_0 = 1500$ K and $T_1 = 1236$ K, for 0.1 μm grains.

The transition between these two regimes occurs at grain radius 0.5 μm, which yields $T_0 = 1474$ K, $T_1 = 1492$ K, and the maximum temperature of 1500 K at $\tau_V = 0.34$.

A4. DISK RIM RADIUS AND NEAR-IR BUMP STRENGTH

Since the rim optical depth is large, we can assume that both temperatures T_0 and T_1 are located at essentially the same distance from the star. If we set T_1 to the dust sublimation temperature $T_{\rm sub}$, then based on equation (A4), the rim radius is

$$R_{\rm rim} = \frac{1}{2} R_* \left(\frac{T_*}{T_{\rm sub}}\right)^2 \sqrt{2\frac{\sigma_{\rm IR}}{\sigma_V} + 1 + 2\frac{\sigma_V}{\sigma_{\rm IR}} e^{-1}} \sqrt{1 + H_{\rm rim}/R_{\rm rim}}, \tag{A7}$$

where we used $F_* = L_*(1 + H_{\rm rim}/R_{\rm rim})^{1/2}/4\pi R_{\rm rim}^2$ [the factor $(1 + H_{\rm rim}/R_{\rm rim})^{1/2}$ is correction for rim self-irradiation, already introduced by DDN01]. Comparison with equation (4) for the rim radius gives

$$\psi = \frac{2}{e} + \frac{\sigma_{\rm IR}}{\sigma_V}\left(1 + 2\frac{\sigma_{\rm IR}}{\sigma_V}\right). \tag{A8}$$

The two extreme opacity regimes yield

$$\psi \sim \begin{cases} 1 & \text{when } \sigma_{\rm IR}/\sigma_V \ll 1 \text{ (nongray dust)} \\ 4 & \text{when } \sigma_{\rm IR}/\sigma_V \to 1 \text{ (gray dust)} \end{cases} \tag{A9}$$

This result can also be derived by setting $T_0 \sim T_{\rm sub}$. Combining this result with equations (3) and (4) and dividing the overall observed flux at 2 μm by the stellar flux at 1 μm yields the near-IR bump strength

$$\frac{F_{2\ \mu{\rm m}}}{F_{1\ \mu{\rm m}}} = \frac{B_{2\ \mu{\rm m}}(T_*)}{B_{1\ \mu{\rm m}}(T_*)} + \left(\frac{T_*}{T_{\rm rim}}\right)^4 \frac{B_{2\ \mu{\rm m}}(T_{\rm rim})}{B_{1\ \mu{\rm m}}(T_*)} \frac{H_{\rm rim}}{\pi R_{\rm rim}}\left(1 + \frac{H_{\rm rim}}{R_{\rm rim}}\right) \times \begin{cases} 1 & \text{nongray dust} \\ 4\sin i & \text{gray dust} \end{cases}, \tag{A10}$$

where we used the approximation $q_\lambda \sim \sigma_{\rm IR}/\sigma_V \sim \bar{\sigma}(T_{\rm rim})/\bar{\sigma}(T_*)$. This solution shows that nongray dust gives angle-independent bump strength in addition to reducing its magnitude from the gray dust result.

REFERENCES

Allen, D. A. 1973, MNRAS, 161, 145
Augereau, J. C., Lagrange, A. M., Mouillet, D., & Ménard, F. 2001, A&A, 365, 78
Berrilli, F., Corciulo, G., Ingrosso, G., Lorenzetti, D., Nisini, B., & Strafella, F. 1992, ApJ, 398, 254
Berrilli, F., Lorenzetti, D., Saraceno, P., & Strafella, F. 1987, MNRAS, 228, 833
Bouchet, P., & Swings, J. P. 1982, in IAU Symp. 98, Be Stars, ed. M. Jaschek & H.-G. Groth (Dordrecht: Reidel), 241
Bouwman, J., de Koter, A., van den Ancker, M. E., & Waters, L. B. F. M. 2000, A&A, 360, 213
Chiang, E. I. & Goldreich, P. 1997, ApJ, 490, 368 (CG)
Chiang, E. I., et al. 2001, ApJ, 547, 1077
Cohen, M. 1973a, MNRAS, 161, 85
———. 1973b, MNRAS, 161, 97
———. 1973c, MNRAS, 161, 105
———. 1975, MNRAS, 173, 279
———. 1980, MNRAS, 191, 499
Cohen, M., & Schwartz, R. D. 1976, MNRAS, 174, 137
Corder, S., Eisner, J., & Sargent, A. 2005, ApJ, 622, L133
de Winter, D., van den Ancker, M. E., Maira, A., Thé, P. S., Djie, H. R. E. T. A., Redondo, I., Eiroa, C., & Molster, F. J. 2001, A&A, 380, 609
Dominik, C., Dullemond, C. P., Waters, L. B. F. M., & Walch, S. 2003, A&A, 398, 607
Dorschner, J., Begemann, B., Henning, T., Jaeger, C., & Mutschke, H. 1995, A&A, 300, 503
Dullemond, C. P. 2002, A&A, 395, 853
Dullemond, C. P., & Dominik, C. 2004, A&A, 417, 159 (DD04)
Dullemond, C. P., Dominik, C., & Natta, A. 2001, ApJ, 560, 957 (DDN01)
Eiroa, C., et al. 2002, A&A, 384, 1038
Eisner, J. A., Lane, B. F., Akeson, R. L., Hillenbrand, L. A., & Sargent, A. I. 2003, ApJ, 588, 360
Eisner, J. A., Lane, B. F., Hillenbrand, L. A., Akeson, R. L., & Sargent, A. I. 2004, ApJ, 613, 1049
Fouqué, P., Le Bertre, T., Epchtein, N., Guglielmo, F., & Kerschbaum, F. 1992, A&AS, 93, 151
Fukagawa, M., et al. 2004, ApJ, 605, L53
Garcia-Lario, P., Manchado, A., Pych, W., & Pottasch, S. R. 1997, A&AS, 126, 479
Gillett, F. C., & Stein, W. A. 1971, ApJ, 164, 77
Glass, I. S., & Penston, M. V. 1974, MNRAS, 167, 237
Gómez, J. F., & D'Alessio, P. 2000, ApJ, 535, 943
Grady, C. A., et al. 1999, ApJ, 523, L151
———. 2000, ApJ, 544, 895
———. 2001, AJ, 122, 3396
———. 2003, PASP, 115, 1036
———. 2005, ApJ, 620, 470
Hanner, M. 1988, Infrared Observations of Comets Halley and Wilson and Properties of the Grains (Washington: NASA), 22
Herbst, W., & Shevchenko, V. S. 1999, AJ, 118, 1043
Hillenbrand, L. A., Strom, S. E., Vrba, F. J., & Keene, J. 1992, ApJ, 397, 613
Hu, J. Y., Thé, P. S., & de Winter, D. 1989, A&A, 208, 213
Hutchinson, M. G., et al. 1994, A&A, 285, 883
Ivezić, Ž., & Elitzur, M. 1997, MNRAS, 287, 799
Ivezić, Ž., Nenkova, M., & Elitzur, M. 1999, User Manual for DUSTY (Lexington: Univ. Kentucky), http://www.pa.uky.edu/~moshe/dusty
Kilkenny, D., Whittet, D. C. B., Davies, J. K., Evans, A., Bode, M. F., Robson, E. I., & Banfield, R. M. 1985, South African Astron. Obs. Circ., 9, 55
Kolotilov, E. A., Zaitseva, G. V., & Shenavrin, V. I. 1977, Astrofizika, 13, 449
Kurucz, R. 1969, ApJ, 156, 235
Lawrence, G., Jones, T. J., & Gehrz, R. D. 1990, AJ, 99, 1232
Li, W., Evans, N. J., Harvey, P. M., & Colome, C. 1994, ApJ, 433, 199
Liu, W. M., Hinz, P. M., Hoffmann, W. F., Brusa, G., Miller, D., & Kenworthy, M. A. 2005, ApJ, 618, L133
Liu, W. M., Hinz, P. M., Meyer, M. R., Mamajek, E. E., Hoffmann, W. F., & Hora, J. L. 2003, ApJ, 598, L111
Lorenzetti, D., Saraceno, P., & Strafella, F. 1983, ApJ, 264, 554
Low, F. J. 1970, AFCRL-70-0179 (Bedford: AFCRL)
Malbet, F. 2003, Ap&SS, 286, 131
Malfait, K., Bogaert, E., & Waelkens, C. 1998, A&A, 331, 211
Mannings, V., & Sargent, A. I. 1997, ApJ, 490, 792
Millan-Gabet, R., Schloerb, F. P., & Traub, W. A. 2001, ApJ, 546, 358
Miroshnichenko, A., Ivezić, Ž., Vinković, D., & Elitzur, M. 1999, ApJ, 520, L115
Monnier, J. D., & Millan-Gabet, R. 2002, ApJ, 579, 694
Monnier, J. D., et al. 2005, ApJ, 624, 832
Muzerolle, J., Calvet, N., Hartmann, L., & D'Alessio, P. 2003, ApJ, 597, L149
Olnon, F. M., et al. 1986, A&AS, 65, 607
Piétu, V., Guilloteau, S., & Dutrey, A. 2005, A&A, in press (astro-ph/0504023)
Prusti, T., Natta, A., & Palla, F. 1994, A&A, 292, 593
Schneider, G., et al. 2003, AJ, 125, 1467
Semenov, D., Pavlyuchenkov, Y., Schreyer, K., Henning, T., Dullemond, C., & Bacmann, A. 2005, ApJ, 621, 853
Sylvester, R. J., Skinner, C. J., Barlow, M. J., & Mannings, V. 1996, MNRAS, 279, 915
Stapelfeldt, K. R., et al. 2003, ApJ, 589, 410
Strom, K. M., et al. 1989, ApJS, 71, 183
Strom, S. E., Strom, K. M., Yost, J., Carrasco, L., & Grasdalen, G. 1972, ApJ, 173, 353
Thé, P. S., Cuypers, H., Tjin A Djie, H. R. E., & Felenbok, P. 1985, A&A, 149, 429
Tjin A Djie, H. R. E., Remijn, L., & Thé, P. S. 1984, A&A, 134, 273
van Boekel, R., et al. 2003, A&A, 400, L21
———. 2005, A&A, 437, 189
van den Ancker, M. E., Bouwman, J., Wesselius, P. R., Waters, L. B. F. M., Dougherty, S. M., & van Dishoeck, E. F. 2000, A&A, 357, 325
Vinković, D., Ivezić, Ž., Miroshnichenko, A. S., & Elitzur, M. 2003, MNRAS, 346, 1151 (V03)
Yudin, R. V. 2000, A&AS, 144, 285
Weigelt, G., Balega, Y. Y., Hofmann, K.-H., & Preibisch, T. 2002, A&A, 392, 937
Wolf, S. 2003, ApJ, 582, 859